



Cite this: DOI: 10.1039/d5ta02325d

Negative linear compressibility and complex phase behaviour in  ${}^7\text{Li}_2\text{CO}_3$ †Christopher J. Ridley, \*<sup>ab</sup> Fabio Orlandi, <sup>b</sup> Craig L. Bull, <sup>bc</sup> Nicholas P. Funnell, <sup>b</sup> Jasmine K. Hinton, <sup>a</sup> Robin S. Perry, <sup>bd</sup> Stephen Hull <sup>b</sup> and Rebecca Wurr ‡<sup>b</sup>

We present a combination of neutron powder-diffraction measurements demonstrating negative linear compressibility and irregular thermal expansion in  ${}^7\text{Li}_2\text{CO}_3$ . This is shown to be due to an interplay between the tilting of the rigid carbonate group and the shear strain in the unit cell, which leads to a first-order transition from monoclinic to hexagonal symmetry. The phase evolution is shown to be highly sensitive to the level of hydrostaticity in the sample. Under hydrostatic conditions, the sample begins transformation at 8.5 GPa leading to a change from tetrahedral to octahedral Li coordination. Symmetry adapted basis mode analysis, combined with density functional theoretical (DFT) calculations and Raman spectroscopy, is used to show that this transition is reverse ferroelastic in nature.

Received 21st March 2025  
Accepted 12th May 2025

DOI: 10.1039/d5ta02325d

rsc.li/materials-a

## Introduction

Alkali metal-carbonates are a family of industrially important materials. They are used in the production of detergents, glass and ceramic manufacture, pharmaceuticals, and in energy applications.  $\text{Li}_2\text{CO}_3$  is the largest global source of Li-metal, predominantly used for the production of cathode materials such as  $\text{LiCoO}_2$ , for the manufacture of Li-ion batteries.  $\text{Li}_2\text{CO}_3$  is also used as the dominant electrolyte component in molten-carbonate fuel cells (forming a eutectic with  $\text{K}_2\text{CO}_3$ ), which are of growing interest for generating power and capturing  $\text{CO}_2$  from the flue gases emitted by natural gas power plants, or other carbon-intensive processes.<sup>1</sup> Other applications include  $\text{CO}_2$  sensing,<sup>2</sup> and as a non-metallic catalyst for diamond synthesis.<sup>3</sup>

The crystallographic structure of  $\text{Li}_2\text{CO}_3$  at ambient conditions was first reported by Zemann<sup>4</sup> from single-crystal X-ray diffraction (XRD), and later reconfirmed by Effenberger and Zemann.<sup>5</sup> The symmetry is  $C2/c$  (see Fig. 1), with the main structural feature being a staggered off-set arrangement of  $\text{CO}_3^{2-}$  groups along the  $c$ -axis. This forms layers along the  $a$ -

axis, separated by layers of slightly distorted, tetrahedrally coordinated Li atoms. The tetrahedra each have one shared-edge within the layers, and two shared-corners between the layers, one of which meets at the shared edge of another pair of tetrahedra. This forms a canted bow-tie arrangement within the layers of Li–O tetrahedral units, with the bow-ties alternating in orientation with translation along the  $c$ -axis.

The related compound,  $\text{Na}_2\text{CO}_3$ , is well known for being the only incommensurately modulated alkali-carbonate in the  $\gamma$ -phase at room temperature.<sup>6</sup> This transforms to a commensurately modulated  $\delta$ -phase below 170 K, with both modulated phases possessing the same monoclinic average symmetry ( $C2/m$ ).<sup>7</sup> On heating, the amplitude of the modulation drops to zero, transforming to the  $\beta$ -phase above 620 K, maintaining monoclinic symmetry ( $C2/m$ ). With further heating above 763 K, the hexagonal ( $P6_3/mmc$ )  $\alpha$ -phase forms.<sup>8,9</sup> Doping with Li,  $\text{LiNaCO}_3$  forms a triclinic structure which has a complex phase diagram driven by differing tetrahedrally coordinated  $\text{Li}^+$  and distorted square-pyramidal coordinated  $\text{Na}^+$  ions.<sup>10</sup> The triclinic phase transforms to a hexagonal phase above 448 K,<sup>10,11</sup> with an order-disorder transition to another hexagonal phase above 633 K, resulting in two distinct  $\text{CO}_3^{2-}$  environments.<sup>12</sup> Upon doping with K, forming  $\text{LiKCO}_3$ , the Li is forced into a  $\text{LiO}_5$  pyramidal coordination, alongside the  $\text{KO}_9$  polyhedra, maintaining monoclinic symmetry.<sup>13,14</sup>

Studies into the effects of high-temperature on the structure of  $\text{Li}_2\text{CO}_3$  are complicated by its chemical-reactivity, and the formation of eutectics with trace impurities. Differential thermal-analysis (DTA) performed under either a  $\text{CO}_2$  atmosphere or air showed a clear heat-effect at approximately 683 K prior to melting at 993 K, indicative of a solid–solid transition.<sup>15</sup> In air, additional features in the DTA suggested the formation of

<sup>a</sup>Neutron Scattering Division, Oak Ridge National Laboratory, Oak Ridge, TN, USA. E-mail: ridleycj@ornl.gov

<sup>b</sup>ISIS Neutron and Muon Source, Rutherford Appleton Laboratory, Chilton, Didcot OX11 0QX, UK

<sup>c</sup>School of Chemistry, University of Edinburgh, David Brewster Road, Edinburgh EH9 3FJ, UK

<sup>d</sup>London Centre for Nanotechnology and Department of Physics and Astronomy, University College London, Gower Street, London WC1E 6BT, UK

† Electronic supplementary information (ESI) available. See DOI: <https://doi.org/10.1039/d5ta02325d>

‡ Present address: Department of Physics, King's College London, London WC2R 2LS, UK.



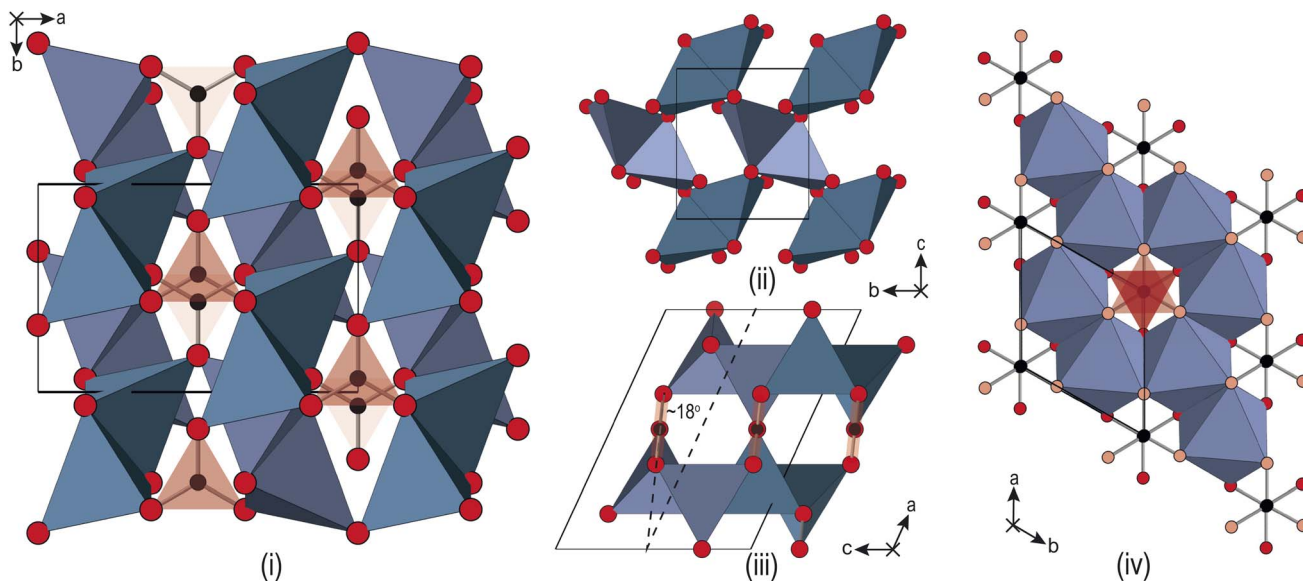


Fig. 1 Overview of the ambient temperature structures of Li<sub>2</sub>CO<sub>3</sub>. The red and black spheres are O and C atoms respectively, and the blue/shaded polyhedra are Li–O<sub>4/6</sub> units, depending on the phase. (i) The ambient-pressure monoclinic (C2/c) form, viewed along the c-axis shows the staggered stacking of the CO<sub>3</sub><sup>2-</sup> groups, and the arrangement of paired edge-shared Li-tetrahedra around them. (ii) The edge-shared Li-tetrahedra form a canted 'bow-tie' arrangement when viewed along the a-axis. (iii) When viewed in the ac-plane the CO<sub>3</sub><sup>2-</sup> groups are tilted ~18° relative to the a-axis. (iv) The hexagonal (P6<sub>3</sub>/mcm) phase, at 11.1 GPa, showing that the CO<sub>3</sub><sup>2-</sup> groups are no longer staggered in the ab-plane and are perpendicular to the c-axis. The large displacement in the Li atoms results in a change in coordination, forming Li–O<sub>6</sub> octahedra. The octahedra form edge-shared rings around the CO<sub>3</sub><sup>2-</sup> groups in the ab-plane, while neighbouring rings along the c-axis are face-shared, forming continuous chains.

a eutectic with Li<sub>2</sub>O, indicating that the loss of CO<sub>2</sub> from the sample causes premature decomposition.<sup>15</sup> This effect was observed again in a later study by Klement Jr and Cohen,<sup>16</sup> with the sample in air. A structural study, using high-temperature powder XRD, further considered the effects of sample history and atmosphere on the occurrence of a possible solid–solid transition.<sup>17</sup> Khlapova and Kovaleva<sup>17</sup> concluded that Li<sub>2</sub>CO<sub>3</sub> exists in three crystalline forms under ambient conditions: the stable monoclinic α-form, the metastable β-form (of unknown symmetry) which may be recovered from the melt (melting temperature 993 K<sup>18</sup>) where the sample isn't subsequently exposed to moisture or CO<sub>2</sub>, and the γ-form upon heating above 681 K. However, the presence of 0.91% trace impurities in the sample may explain these transitions, potentially with a ternary eutectic with Na<sub>2</sub>CO<sub>3</sub> and K<sub>2</sub>CO<sub>3</sub> as suggested by Stober.<sup>18</sup>

The predominant interest in the application of high-pressure to the alkali-metal carbonates is in the search for an sp<sup>3</sup>-bonded structure, analogous to those observed for alkaline-earth carbonates.<sup>19</sup> Both Na<sub>2</sub>CO<sub>3</sub> and K<sub>2</sub>CO<sub>3</sub> have been shown to have rich high-pressure phase-diagrams.<sup>20–24</sup> While some of the early DTA work considered the application of modest hydrostatic pressures to Li<sub>2</sub>CO<sub>3</sub>,<sup>16</sup> it has received relatively little attention compared with the other carbonates. The focus in the literature is on the use of the material as a non-metallic catalyst for diamond synthesis, with a view to increasing the purity of the end-product.<sup>3</sup> Grzechnik *et al.*<sup>25</sup> also considered this, and were the first to study the structural changes in Li<sub>2</sub>CO<sub>3</sub> with pressure. A new high-pressure hexagonal phase (P6<sub>3</sub>/mcm) was identified, see Fig. 1(iii) and (iv), with phase coexistence

between 10–18 GPa. However, there were a number of additional features observed in the diffraction patterns, suggesting that there may be unidentified phases in the lower pressure regime, up to 6 GPa. Likely limited by the appearance of unindexed peaks, Grzechnik *et al.*<sup>25</sup> did not report any structural analysis of the high pressure data prior to the phase transition.

In the synthesis of Li-based cathode materials, such as Ni-doped LiCoO<sub>2</sub> compounds, the presence of unreacted Li<sub>2</sub>CO<sub>3</sub> can be problematic, resulting in additional cation disorder resulting in rapid capacity fade.<sup>26</sup> The application of high-pressure during synthesis has the potential to lead to better conversion, though a better understanding of how Li<sub>2</sub>CO<sub>3</sub> itself behaves under pressure is needed first. The present study uses neutron powder-diffraction data, combined with Raman spectroscopy and computation, to better understand the structural properties of this material under high-pressures and -temperatures.

## Experimental details

Polycrystalline Li<sub>2</sub>CO<sub>3</sub> with 99.95 at% <sup>7</sup>Li was supplied by Oak Ridge National Laboratory (ORNL, USA). The isotopic <sup>7</sup>Li enrichment reduces the level of neutron absorption, improving the measured signal. No crystalline impurities were observed in the neutron diffraction patterns at ambient conditions, demonstrating high chemical-purity in the bulk compound. Single crystals of natural <sup>6</sup>Li<sub>2</sub>CO<sub>3</sub> were grown using a modified floating zone technique. Neutron diffraction measurements were performed using the PEARL diffractometer at the ISIS



Neutron and Muon Source,<sup>27</sup> and the SNAP diffractometer at Oak Ridge National Laboratory. Vibrational spectroscopy calculations were performed using the plane-wave DFT package, CASTEP 23.1.<sup>28</sup> ISODISTORT and the ISOTROPY suite were used for the symmetry mode analysis.<sup>29,30</sup> Full experimental details are available in the ESI.†<sup>31–39</sup>

## Results and discussion

### Structural changes upon heating

Fig. 2(i) shows the neutron powder-diffraction pattern from the sample at ambient conditions; no traces of crystalline impurity were observed, and refining the monoclinic ( $C2/c$ ) structure against these data results in a good fit. The refined model is listed in Table 1. The lattice parameters compare favourably with previous reports.<sup>26</sup> The sample maintained this monoclinic

structure over the full temperature range investigated 4–850 K, the refined structures at 4 K and 850 K are also listed in Table 1. Upon heating, the unit cell preferentially expands in the  $ac$ -plane, with an increase in the  $\beta$ -angle, and the  $b$ -axis remaining essentially invariant, reducing slightly at higher temperatures, see Fig. 2(ii). This is clearly seen in the diffraction patterns, see inset Fig. 2(ii), with the splitting of the  $(\bar{2}02)$  and  $(111)$  reflections at approximately 3 Å. The  $(111)$  reflection is close to invariant, while the  $(\bar{2}02)$  shifts significantly to higher  $d$ -spacing on heating.

Above 750 K two additional reflections were observed at 2.37 & 3.35 Å, corresponding to the formation of  $\text{Li}_2\text{O}$  and Si from labile Li reacting with the quartz ampule. These peaks remained in the diffraction pattern after cooling back to ambient conditions, confirming that the sample had started to decompose rather than transform to a high-temperature phase. Above 550 K the  $b$ -axis begins to contract with further heating, while the unit-cell volume continues to expand. There is a clear change in the volumetric thermal-expansion at this temperature (see ESI†). If the principal axes of expansion are considered, see Fig. 3(i), it is clear that while  $\bar{X}_1$  expands as expected, there are other interesting features within the  $ac$ -plane, and along  $\bar{X}_3$  (the  $b$ -axis), suggestive of some competing effects within the structure. Initially, both  $\bar{X}_2$  and  $\bar{X}_3$  show very little response with heating, with both expanding no more than 0.1% by 500 K, and  $\bar{X}_2$  then contracting back to the room temperature value by 600 K.

Above approximately 650 K,  $\bar{X}_2$  begins to expand while  $\bar{X}_3$  slowly contracts, eventually falling back to the room temperature value at the highest temperature considered. The contraction of  $\bar{X}_2$  is driven by the tilting of the rigid  $\text{CO}_3^{2-}$  groups, which starts to change significantly above 400 K, see Fig. 3(ii). This also contributes to the larger expansion along  $\bar{X}_1$ . The upturn in  $\bar{X}_2$  above 600 K is subsequently caused by increased  $\text{CO}_3^{2-}$  out-of-plane libration, which similarly results in the slow contraction of  $\bar{X}_3$  at higher temperatures still, and is apparent in the refined anisotropic displacement parameter (ADP),  $\beta_{33}$ , for O2, see Fig. 3(ii). This has a coupled effect in  $\beta_{33}$  for the Li atom, which may be thought of as a symmetric stretch of the tetrahedral unit. While the ADPs along the other unit-cell axes show an as-expected growth with temperature, the  $\beta_{33}$  parameters for Li and O2 show significant changes, with their values growing 3–4 times larger than either  $\beta_{11}$ , and  $\beta_{22}$  at 800 K. The tilt and libration of the  $\text{CO}_3^{2-}$  therefore contribute competing effects to the expansion/contraction of  $\bar{X}_2$ .

The carbonate group itself was determined to adopt the ideal geometry, within error, with a O1–C–O2 bond angle of  $120.3(2)^\circ$  at 300 K. The two C–O1 bond lengths were determined to be  $1.2901(14)$  Å, and the single C–O2 bond length to be  $1.268(3)$  Å. The O1–C–O2 bond angle remained constant on heating, within error, while the C–O1 bonds contracted, and the C–O2 bonds elongated, resulting in C–O2 being larger than C–O1. The polarising nature of the  $\text{Li}^+$  on the delocalised electrons in the  $\text{CO}_3^{2-}$  group is smaller than group-II carbonates, but it is still expected that the shorter C–O bond belongs to the O coordinated to fewer  $\text{Li}^+$ , in this case O2 (note this is defined as O1 in work of Effenberger and Zemann<sup>5</sup>). These data suggest that

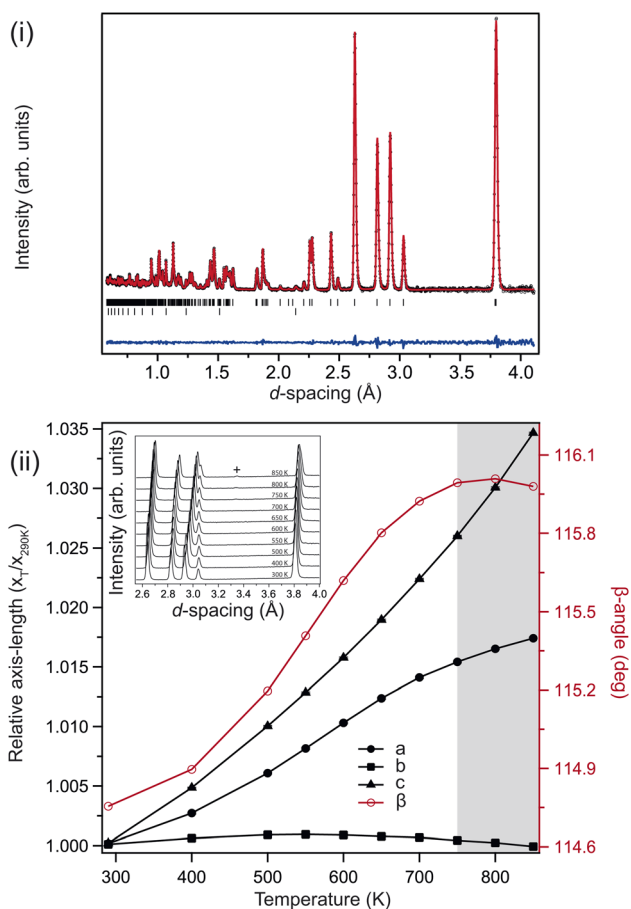


Fig. 2 (i) Ambient-pressure and -temperature neutron powder-diffraction pattern collected from  ${}^7\text{Li}_2\text{CO}_3$ , showing the Rietveld fit to the monoclinic ( $C2/c$ ) structure. The upper tick marks index the sample, the lower tick marks index the small contribution from the V sample container. (ii) Determined changes in lattice parameters for  ${}^7\text{Li}_2\text{CO}_3$  as a function of temperature. Shaded region represents datasets where decomposition is onset. (inset) Diffraction patterns showing the evolution of the region 2.6–4.0 Å with temperature. The two reflections just below and above  $\sim 3$  Å are the  $(\bar{2}02)$  and  $(111)$  reflections respectively. The small reflection marked (+) indicates the appearance of  $\text{Li}_2\text{O}$  above 750 K.



**Table 1** Refined structural parameters from the  $C2/c$  structure of  ${}^7\text{Li}_2\text{CO}_3$  at ambient pressure, representative of the temperature range investigated, 4–850 K. The Li and O1 atoms are on general 8f Wyckoff positions, ( $x, y, z$ ), with the C and O2 atoms on 4e Wyckoff positions, ( $0, y, 1/4$ ). Also shown are the structural parameters from the ambient-pressure relaxed structure from the DFT calculations

	NPD	NPD	NPD	DFT
Temperature (K)	298	850	4	—
$a$ -axis (Å)	8.3613(3)	8.5104(4)	8.3453(4)	8.3248
$b$ -axis (Å)	4.97652(15)	4.9780(2)	4.9747(3)	4.9777
$c$ -axis (Å)	6.1957(2)	6.4130(3)	6.1601(3)	6.1543
$\beta$ -angle ( $^\circ$ )	114.761(2)	115.979(2)	114.6978(15)	114.303
Volume (Å <sup>3</sup> )	234.104(14)	244.23(2)	232.34(2)	232.42
Li- $x$	0.6970(5)	0.6819(8)	0.6962(3)	0.6971
Li- $y$	0.0535(8)	0.0533(9)	0.0533(5)	0.0520
Li- $z$	0.3351(6)	0.3081(10)	0.3342(4)	0.3364
C- $y$	0.0652(5)	0.0770(6)	0.0665(3)	0.0654
O1- $x$	0.1470(2)	0.1423(3)	0.14691(12)	0.1472
O1- $y$	0.9369(3)	0.9423(4)	0.9355(2)	0.9345
O1- $z$	0.3132(3)	0.3057(3)	0.31335(14)	0.3135
O2- $y$	0.3209(5)	0.3313(6)	0.3233(3)	0.3220
$\rho$ (g cm <sup>-3</sup> )	2.096	2.010	2.112	2.112

approaching decomposition, it is this shorter C–O oxygen which eventually forms an oxide ion with Li, and the initially less delocalised O1 atoms which form CO<sub>2</sub>.

An additional measurement was performed at 4 K, where the sample was observed to maintain monoclinic symmetry. A simple two point analysis of the changes in the unit cell, suggests that the principal axes contract as expected on cooling.

### High-pressure phase transitions: how many are there?

The previous study observed a series of phase transitions, of unknown symmetry or structure, with increasing pressure up to 6 GPa.<sup>25</sup> It is possible that these phases are not thermodynamically stable, instead being induced through non-hydrostatic pressure conditions. We have investigated this further through varying the ratio of pressure-medium to sample in the gasket. Three cases were tested: (1) the sample was firmly packed into the gasket, with the remaining voids in the sample space filled with pressure medium; (2) the sample was initially pelletised, and then compressed without pressure medium; (3) the sample was loosely packed into the gasket, with a greater volume of pressure medium.

In case 1, a single unaccounted-for reflection was observed to grow into the diffraction patterns at  $\sim 2.32$  Å above  $\sim 3.8$  GPa (see Fig. 4 and ESI†). Additionally, the intensity of the (112) reflection is seen to grow significantly in intensity, unaccounted for by the current crystallographic model. The additional reflection is unindexed by the existing cell, or alternative cells common to other alkali-metal carbonates. Loss of the  $c$ -glide and  $C$ -centering were also checked; the peak remains unindexed against metrically similar monoclinic cells with  $C2$ ,  $P2$ ,  $P2_1$ ,  $P2_1/c$  symmetry. It may be related to the (210) reflection of the high-symmetry hexagonal phase, though at significantly lower pressures (reported above 10 GPa<sup>25</sup>). Attempts to freely index the new pattern suggest that a loss of  $C$ -centering, an increase in  $\beta$ -angle, and a  $\sim 2.5\times$  elongation of the  $c$ -axis may fit the data, though no structure could be found.

In case 2, the pelletisation led to no adverse changes in the initial pattern (see ESI†), with no significant broadening or preferred orientation. As the pressure is increased the sample peaks are initially seen to broaden and reduce in intensity, consistent with growing levels of strain. Several reflections are seen to shift at different rates to those in case 1. For example, the cluster of reflections (311)/(020)/(112̄)/(002) merge together, as in case 1, but the (002) reflection then shifts to much lower  $d$ -spacing with a larger relative intensity, see Fig. 4. The hexagonal phase is also induced at lower pressures than in the hydrostatic case. If the positions of the (200)/(110) are compared between case 1 and 2, the hexagonal phase is seen to emerge at a significantly lower pressure of approximately 5.2 GPa. A similar effect is seen in the Raman data. The diamond anvil cell (DAC) loading is tightly packed with sample (similar to case 1), and the structural change is clearly mirrored in the Raman spectra, onset above approximately 5 GPa (see ESI†). The allowed Raman modes in each phase were confirmed through DFT phonon calculations (the CASTEP output for these is included as ESI†). Experimentally, there remain some features that are forbidden in the hexagonal symmetry, suggesting that when highly strained the sample locally retains some monoclinic character.

In case 3, the sample reflections behave similarly to case 1, but with no additional reflections observed (see ESI†). Comparing the relative intensity of the nearest expected reflection between the over- and under-packed cases demonstrates that, even with differing signal to background, the reflection is clearly absent. In all three cases, the sample fully reverts to the ambient monoclinic structure on pressure release. It is therefore clear that the sample is highly sensitive to the level of deviatoric stress in the pressure environment. As the additional peak cannot be accounted for with any obvious loss of symmetry, it is possibly the result of domain structure in the sample, only apparent where the powder density is increased above a critical threshold. The single-crystal XRD



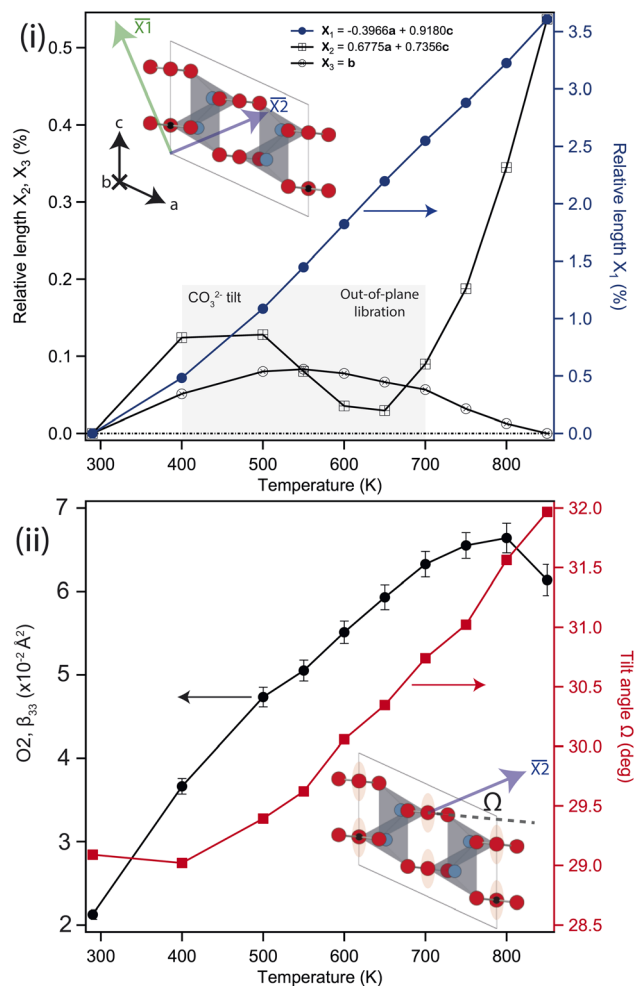


Fig. 3 (i) Change in principal axis lengths relative to their values at 300 K.  $\bar{X}_3$  is parallel to the  $b$ -axis,  $\bar{X}_1$  and  $\bar{X}_2$  lay in the  $ac$ -plane, as shown in the inset figure. The shaded region represents the temperature region where the interplay between the carbonate tilt and out-of-plane libration is important (see main text) (ii) temperature dependence of the anisotropic displacement parameter (ADP),  $\beta_{33}$ , of the O2 atom (illustrated by ellipsoids on inset). Only  $\beta_{33}$  shows a dramatic change with temperature, with  $\beta_{11}$ ,  $\beta_{22}$  and  $\beta_{13}$  not rising above  $\sim 2 \times 10^{-2} \text{ \AA}^2$ . Also shown is the change in angle  $\Omega$  with temperature, defined as the angle between the  $\text{CO}_3^{2-}$  plane and  $\bar{X}_2$  (see inset).

measurements confirmed that the monoclinic structure is stable where the pressure conditions are hydrostatic, with no unindexed reflections.

This sensitivity to non-hydrostatic pressure is consistent with the observations of Grzechnik *et al.*,<sup>25</sup> who used a DAC to apply pressure under non-hydrostatic conditions. The uniaxial strain field in a DAC is very different to that in a toroidal anvil assembly. In the latter, it has been shown that a pellet of NaCl at 6 GPa can sustain uniaxial stresses of the order 0.3 GPa.<sup>40</sup>  $\text{Li}_2\text{CO}_3$ , having a slightly larger shear-modulus than NaCl, is expected to sustain higher levels than this. A DAC loading is geometrically more uniaxial, and this results in a very different evolution of the structure. This is evidenced by the fact that at 5 GPa we see the early onset of the hexagonal structure, which is not observed in the previous DAC measurements. It would be an

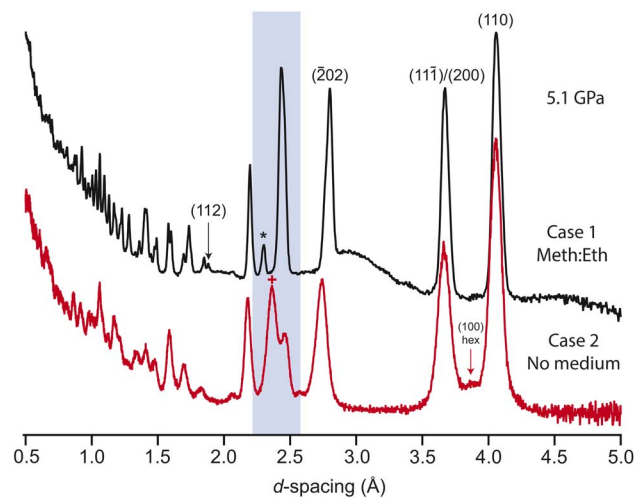


Fig. 4 Comparing cases 1 and 2. Measured on the SNAP diffractometer. The upper plot (black) is collected with a hydrostatic medium generating 5.1 GPa (the broad feature in the background is from the liquid medium). The lower dataset (red) is collected without any hydrostatic medium. Based on the position of the (200)/(110) reflections, this is estimated to be an equivalent pressure. The first signs of the high-pressure phase is the hexagonal (100) emerging between the monoclinic (200)/(110) reflections in the lower plot. Cases 1 and 3 look identical at these pressures apart from the appearance of the single unindexed reflection marked \*, and the strong intensity change in the (112) reflection (see main text). The highlighted region represents the cluster of (311)/(020)/(112)/(002) merged under a single peak. In the lower plot, the (002) is seen to have shifted significantly further to lower  $d$ -spacing, marked with +. Note that the position of the (202) reflection at  $\sim 2.7 \text{ \AA}$  does not match.

interesting future study to consider the effects of uniaxial stress on a single-crystal.

The data discussed in the remainder of this study were collected from loadings where the gaskets were packed less firmly, loaded with a larger volume of pressure medium (as per case 3). The sample is therefore considered to be under hydrostatic conditions up to 10.5 GPa, the limit of methanol : ethanol (4 : 1 by volume) at room temperature.<sup>41</sup> Fig. 5(i) shows a representative high-pressure data set from  $\text{Li}_2\text{CO}_3$  at 4.1 GPa. The monoclinic phase was found to be stable up to 8.5 GPa. Beyond this, additional reflections appeared in the pattern corresponding to the hexagonal phase, most notably the (100) reflection at approximately 3.88  $\text{\AA}$ . The monoclinic and hexagonal phases coexisted, with the hexagonal phase-fraction increasing up to approximately 10 GPa, beyond which the sample was purely hexagonal.

### Negative linear compressibility

The change in unit-cell volume (inset, Fig. 5(i), residual plot in ESI†) is described using a Rydberg–Vinet equation of state (EOS), with  $V_0 = 234.24(14) \text{ \AA}^3$ ,  $B_0 = 31.5(8) \text{ GPa}$  and  $B_p = 5.0(3)$ , in good agreement with the ambient pressure unit-cell volume listed in Table 1. While the unit-cell volume is well approximated by the EOS, it isn't able to fully reproduce the measured changes below 3 GPa, where there is a clear inflexion in the data, reproduced by both the neutron and XRD measurements.



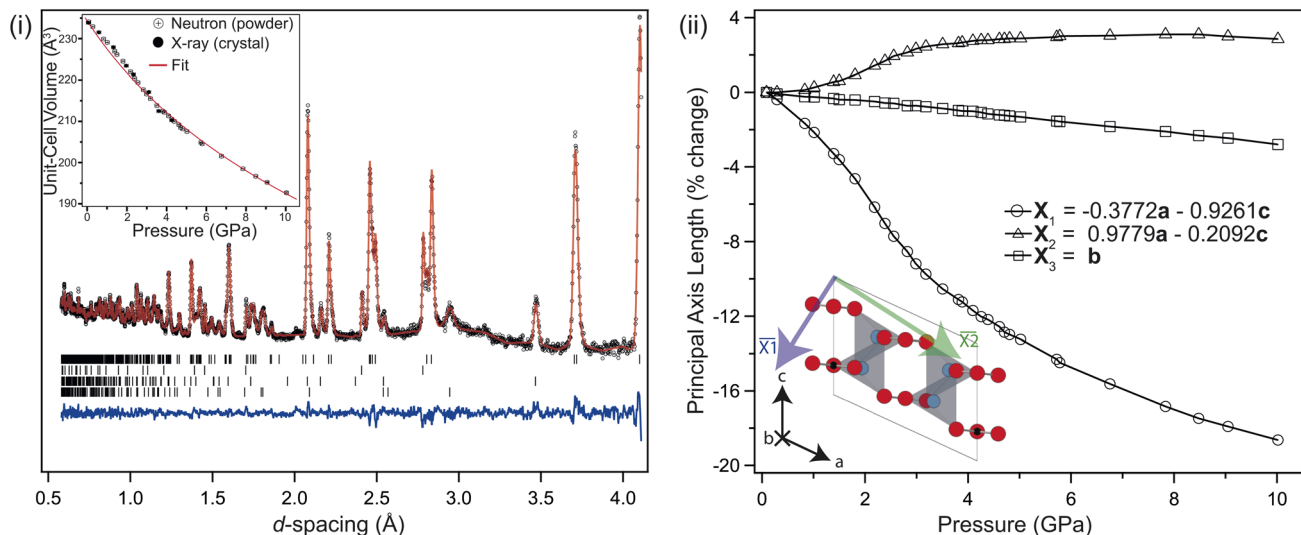


Fig. 5 (i) Neutron diffraction pattern, and Rietveld refined profile for monoclinic  $\text{Li}_2\text{CO}_3$  collected at approximately 4.1 GPa. The black markers are the measured data, the red line is the calculated profile, the lower blue line is the residual to the fit. From top to bottom, the tick marks index monoclinic  $\text{Li}_2\text{CO}_3$ , Pb,  $\text{Al}_2\text{O}_3$  and  $\text{ZrO}_2$  respectively. (inset, i) the determined unit-cell volume as a function of pressure, fitted against a Rydberg–Vincent equation of state, with parameters as described in the main text. The error bars are shown, though are smaller than the data markers. (ii) Percentage change in the principal axes of  $\text{Li}_2\text{CO}_3$  as a function of pressure, orientated as shown in the inset figure.

Looking at the percentage length change in the principal axes with pressure, see Fig. 5(ii);  $\bar{X}_3$  compresses almost linearly, while  $\bar{X}_1$  compresses non-linearly, and  $\bar{X}_2$  expands non-linearly. The balance struck between the nonlinear expansion and contraction of  $\bar{X}_2$  and  $\bar{X}_1$  respectively causes an unusual form to the pressure–volume curve below 4 GPa, which is also seen in the data collected from the single crystal XRD. The cause of this non-linear compression is the interplay between unit-cell shear and tilting of the rigid  $\text{CO}_3^{2-}$  groups within the cell. The tilt of the group relative to the  $a$ -axis is shown in Fig. 6. The linear reduction in tilt-angle results in an effective expansion along the  $a$ -axis, while the non-linear increase in  $\beta$ -angle (equivalent to shear) counteracts this. At higher pressures, the shear dominates, and the unit-cell volume reduces following the expected Rydberg–Vincent trend. The resultant negative compressibility along the  $a$ -axis is  $-3.18 \text{ TPa}^{-1}$  over the 7 GPa range.

The Li–O tetrahedral volume reduces by  $\sim 19.4\%$  up to 10 GPa. The distortion index (deviation in bond length away from the average Li–O bond length) shows no obvious change outside of error up to the on-set of the transition, but then increases from approximately 0.02 to 0.06 between 8 and 10 GPa, as the Li coordination becomes increasingly octahedral.

### Symmetry analysis of the monoclinic–hexagonal transition

The high-pressure form of  $\text{Li}_2\text{CO}_3$  formed above 8.5 GPa is hexagonal (space group:  $P6_3/mcm$ ), see Fig. 1(iv), with edge-shared Li– $\text{O}_6$  octahedra in the  $ab$ -plane. These build face-shared columns along the  $c$ -axis forming an 8-membered ring of Li– $\text{O}_6$  octahedra around each  $\text{CO}_3^{2-}$  group, the central C-atoms of which now sit on the Wyckoff  $2a$  (0,0,1/4) site. The transition from monoclinic to hexagonal is seen to occur gradually, with phase coexistence over a range of  $\sim 2$  GPa,

becoming phase pure hexagonal above  $\sim 10$  GPa. The transition is therefore, first-order in nature.

In addition, the low-symmetry monoclinic structure forms a group-subgroup relationship with the high-symmetry hexagonal phase. This allows us to decompose the structure of the low symmetry phase in terms of the amplitudes of a series of symmetry adapted distortion modes. This was done assuming that the unit cell of the low symmetry phase is obtained by applying the transformation matrix  $(-a - 2b, a, c; \text{origin } 000)$  to the hexagonal unit cell. Decomposing the structure in this way shows that there are three order-parameters,  $\Gamma_5^+$  ( $\alpha, -\sqrt{3}\alpha$ ),  $\Gamma_3^+$  ( $\beta$ ),  $\Gamma_6^+$  ( $\gamma, \frac{\gamma}{\sqrt{3}}$ ). We demonstrate later that  $\Gamma_3^+$  and  $\Gamma_6^+$  are the two primary order-parameters of the phase transition.  $\Gamma_6^+$  is dominated by the shear of the unit cell coupled with the tilting of the  $\text{CO}_3^{2-}$  group, while  $\Gamma_3^+$  has no strain component, instead relating to the change in Li coordination.  $\Gamma_5^+$  is therefore a secondary order parameter, related to the change in centering of the  $\text{CO}_3^{2-}$  groups and orthorhombic strain. The transition is ferroelastic, due to the appearance of a spontaneous shear strain in the low symmetry phase.

### Which order parameter is primary?

Further symmetry analysis allows us to consider the coupling between all the distortion modes;<sup>42,43</sup> the coupling between the three order parameters is trilinear ( $\alpha\beta\gamma$ ), acting as a cubic term in the free-energy expansion. This is consistent with, though not a requirement for, the transition being first-order. Furthermore, the transition may be considered as ferroelastic, as the shear strain in the unit cell shares the symmetry of one of the primary order parameters ( $\Gamma_6^+$ ). However, it isn't clear whether the transition may be considered as proper (where the spontaneous strain is the primary order parameter), as the  $\Gamma_6^+$  order



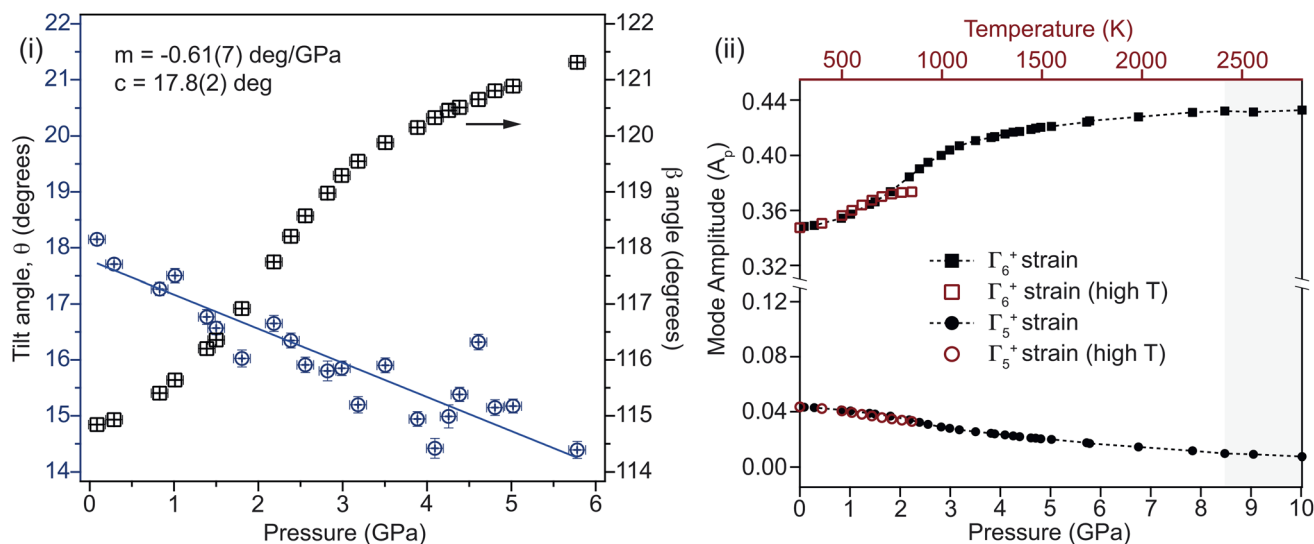


Fig. 6 (i) The angle formed between the plane of the rigid carbonate group against the  $a$ -axis of the unit cell is shown to decrease approximately linearly with pressure (linear fit parameters shown inset). Meanwhile the  $\beta$ -angle (angle between the  $a$ - and  $c$ -axes) is found to increase in a highly non-linear fashion. This balance between tilting of the rigid carbonate group and the increase in shear in the unit cell leads to a small deviation in unit-cell volume around 2 GPa. (ii) Mode amplitudes for the two key strain components relating the low-symmetry monoclinic structure to the hexagonal structure as a function of temperature and pressure, demonstrating that pressure and temperature have a similar effect on the cell distortion.  $\Gamma_6^+$  is a shear strain, while  $\Gamma_5^+$  is an orthorhombic cell distortion. The region of phase coexistence is lightly shaded. Beyond this pressure, both mode amplitudes fall to zero.

parameter has contributions from both homogeneous shear-strain and the tilting of the  $\text{CO}_3^{2-}$  group. The other primary order parameter ( $\Gamma_3^+$ ) has no strain component. From diffraction measurements alone, it is not possible to determine whether the acoustic instability (shear strain) drives the optic instability ( $\text{CO}_3^{2-}$  tilting), or *vice versa*.

DFT calculations were used to disentangle these effects. By considering the relative energetic-stability of structures sequentially deformed from the high-symmetry phase, we are able to show that the transition is proper. The computational model was validated through three methods: the relaxed structure from DFT is first compared with that from the 4 K neutron measurements (see Table 1); the pressure dependence of the unit-cell parameters were compared with those determined from experiment; the calculated Raman spectra were compared with those measured experimentally. These were in good agreement with those reported previously in the literature.<sup>44–47</sup> All three of these confirm that the pseudopotentials provide an accurate portrayal of the sample over a range of pressures and distortions, reproducing the observed negative linear compressibility (see ESI†). Additionally, the effect of hydrostatic pressure on the final calculated enthalpies of the monoclinic and hexagonal phases shows that the hexagonal phase becomes favourable above 5 GPa (see ESI†). This is in reasonable agreement with the observed onset transition pressure of 8.5 GPa.

Through selectively varying the amplitude of each distortion mode we are able to determine which of these are the true driver for the transition. For these calculations, the volumetric ( $\Gamma_1^+$ ) strain was fixed to the values determined for the ambient structure. Fig. 7 shows the results of the calculated final energies for these distorted structures. Fig. 7 shows that  $\Gamma_5^+$  is

a ‘hard’ mode, with a single minimum around zero mode-amplitude.  $\Gamma_3^+$  and  $\Gamma_6^+$  are both found to be ‘soft’ modes, with an energy minimum at non-zero mode-amplitude, and are

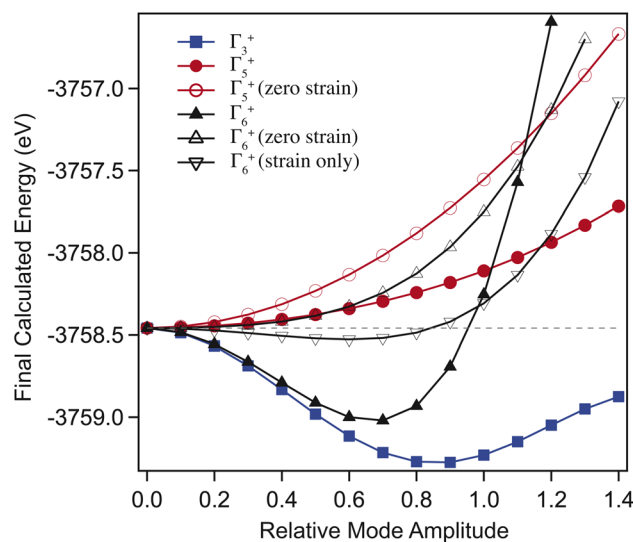


Fig. 7 Final energies, calculated from DFT, comparing the effects of varying the amplitude of the three order parameters  $\Gamma_6^+$  (black triangles),  $\Gamma_3^+$  (blue squares) and  $\Gamma_5^+$  (red circles) in isolation (with the other modes set to zero).  $\Gamma_6^+$  and  $\Gamma_5^+$  are shown with and without the strain component active, additionally  $\Gamma_6^+$  is shown with only the strain component active. The mode amplitude is relative to the relaxed ambient structure amplitude.  $\Gamma_5^+$  shows a single minimum around zero, and is therefore a hard mode.  $\Gamma_3^+$  is a soft mode, showing a minimum at a non-zero amplitude.  $\Gamma_6^+$  is shown to be soft where the strain component is included (with or without atomic displacements), and hard if it is removed.



therefore both primary order-parameters. However, when the strain component of  $\Gamma_6^+$  is set to zero, the mode is switched to being 'hard'. Additionally, where only the strain component of  $\Gamma_6^+$  is varied, it remains 'soft'. This shows that the carbonate group tilt is secondary, and that it is the shear strain that drives the transition, such that it is a proper ferroelastic. DFT also confirms that  $\Gamma_5^+$  is a secondary order parameter induced by  $\Gamma_3^+/\Gamma_6^+$  through the trilinear invariant described previously. Formally, the transition may be considered 'reverse ferroelastic', where the low symmetry monoclinic structure transforms to a higher density, higher symmetry, hexagonal form on applied pressure. An improper example of this is seen in  $\text{Pb}_3(\text{PO}_4)_2$ , where local displacement of the Pb atoms break the symmetry.<sup>48</sup> This is in contrast to the related compound  $\text{Na}_2\text{CO}_3$ , which shows a second-order proper ferroelastic transition, from monoclinic to hexagonal on heating.<sup>9</sup>

### Comparing the effects of pressure and temperature

The effects of temperature and pressure are similar for both  $\Gamma_5^+$  and  $\Gamma_6^+$  strain modes, though over different energy scales (see Fig. 6(ii)). The former reduces with increasing pressure and temperature, while the latter increases in a highly non-linear manner (see ESI<sup>†</sup>). Comparing the mode decomposition results between the temperature and pressure data allows for an estimation of the temperature at which the transition would occur at ambient pressure. This would not be expected to occur below 2400 K which is far in excess of the melting temperature for  $\text{Li}_2\text{CO}_3$  at ambient pressure. Additionally, this implies that heating the sample to 850 K effectively reduces the transition pressure by  $\sim 2$  GPa. Additional high-pressure and -temperature data are needed to draw a more complete comparison.

It is required that the magnitude of the order parameters reduce to zero in the high-symmetry phase, discontinuously in the case of a first-order transition. On the approach to the transition, a gradual reduction in magnitude is indicative of a reduction in stability of the low symmetry phase. In the case of  $\text{Li}_2\text{CO}_3$ , both primary order parameters are found to increase in magnitude on approach to the transition, showing that an increase in distortion of the cell is initially more energetically favourable. This implies that there are competing effects within the structure. Fig. 7 shows that while  $\Gamma_6^+$  shear strain is the 'soft' component, the addition of  $\text{CO}_3^{2-}$  tilting softens the mode further. This suggests that the energetic coupling between these two components is complex, and that while the tilt is not the primary driver of the transition, it certainly has a strong affect on how the structure evolves before it. Given the observed effects of non-hydrostatic pressure, it is possible that uniaxial strain tunes this balance differently, resulting in a new phase which is closely related to the known monoclinic structure.

## Conclusion

The elusive temperature behaviour of this important mineral,  $\text{Li}_2\text{CO}_3$ , has been reinvestigated. We have shown that the temperature and hydrostatic pressure have similar effects, with an interesting interplay between the lattice behaviour and the

carbonate group tilt on heating, leading to non-linear behaviour in the lattice expansion. We find no evidence of additional high temperature phases, only the eventual decomposition of the carbonate, resulting in a partial reaction between the Li and the quartz holder.

The effects of high pressure on the structure and phase transformation of  $\text{Li}_2\text{CO}_3$  have been investigated in detail through combining neutron diffraction and XRD with Raman spectroscopy and DFT calculations. We have demonstrated that there are only two stable phases of  $\text{Li}_2\text{CO}_3$  under hydrostatic conditions, and we have further proven that the material is extremely sensitive to non-hydrostatic conditions.

Under hydrostatic pressure conditions  $\text{Li}_2\text{CO}_3$  demonstrates negative linear compressibility, a phenomenon not typically expected in such simple minerals, but strongly related to the ferroelastic nature of the phase.<sup>49</sup> This is driven by the tilting of the rigid carbonate groups in the structure, competing with the shearing of the unit cell. This leads to a first order phase transition to a hexagonal structure, starting above 8.5 GPa, where the lithium becomes octahedrally coordinated. While the tilting of the carbonate groups is critical to the negative linear compressibility, the transition is accompanied by a large shear strain. The nature of this phase transition was analysed through combining symmetry analysis with DFT calculation, decoupling these two observed changes in the structure, demonstrating that it is a proper ferroelastic transition. This being the case, where one of the primary order-parameters is the shear of monoclinic unit cell, the high sensitivity to externally applied shear-strains is understandable.

The tunability of  $\text{Li}_2\text{CO}_3$  under both hydrostatic and non-hydrostatic pressure has implications for the synthesis of  $\text{LiCoO}_2$ , and other cathode materials. Applying pressure can enable the formation of new phases, often with stoichiometries which are unstable at ambient conditions. This has the potential for improving battery performance, enhancing stability and capacity. The use of pressure may also have interesting applications in the synthesis of novel 'lattice-engineered' compounds, as an alternative to ball-milling,<sup>50</sup> and on new techniques for extracting Li, and the carbonate itself, from other precursors.<sup>51</sup>

For example, high-pressure and -temperature conditions can be used to stabilise new structures which can be recovered back to ambient conditions, such as the case with  $\text{FePO}_4$ .<sup>52,53</sup> This can fundamentally alter the ability for Li to intercalate within a material, and the resultant diffusion pathways.  $\text{LiFePO}_4$  is a well known example of a 'two-phase' Li-intercalation compound, where the Li-concentration results in a phase-transformation in the parent compound.<sup>54</sup> Pressure can be used to balance the material towards one phase or another in tandem. Negative linear compressibility has the counterintuitive effect of elongating crystal structures along one or more of the principal axes. This could for example, be engineered to either open or close a particular pathway. Aside from diffusion and intercalation, a structural phase transition can alter coordination environments, which may influence the likelihood of unintended reactions within the material during charge/discharge or synthesis, affecting charge capacity.<sup>55</sup>



## Data availability

Data for this article, including the neutron powder diffraction data, are available at <https://doi.org/10.5286/ISIS.E.RB2010781> and <https://doi.org/10.14461/oncat.data/2536722>. Further data supporting this article have been included as part of the ESI,† and crystallographic data for Li<sub>2</sub>CO<sub>3</sub> has been deposited at the CCDC.

## Author contributions

The conceptualisation was performed by C. J. R. The formal analysis was performed by C. J. R. and F. O. The investigation was performed by C. J. R., R. W., J. H., C. L. B. and N. P. F. The original draft was prepared by C. J. R. and was reviewed and edited by C. L. B., F. O., S. H. and N. P. F. Single crystals of the sample were prepared by R. S. P.

## Conflicts of interest

There are no conflicts to declare.

## Acknowledgements

The authors acknowledge the Science and Technology Facilities Council for providing neutron beamtime on the PEARL instrument at the ISIS Neutron and Muon Source,<sup>56</sup> and are grateful to Claire Talbott and Adam Sears (Pressure and Furnace Section, ISIS Neutron and Muon Source) for their assistance in running the high-temperature measurements. We also thank the Materials Characterisation Laboratory at the ISIS Neutron and Muon Source for access to the single-crystal XRD facilities. We acknowledge the computing resources provided the STFC Scientific Computing Department's SCARF cluster. A portion of this research used resources at the Spallation Neutron Source, a DOE Office of Science User Facility operated by the Oak Ridge National Laboratory.<sup>57</sup> The beam time was allocated to the SNAP instrument on proposal number IPTS-28913 and IPTS-34329. This research used resources of the Compute and Data Environment for Science (CADES) at the Oak Ridge National Laboratory, which is supported by the Office of Science of the U.S. Department of Energy under Contract No. DE-AC05-00OR22725.

## Notes and references

- 1 T. A. Barckholtz, K. M. Taylor, S. Narayanan, S. Jolly and H. Ghezal-Ayagh, *Appl. Energy*, 2022, **313**, 118553.
- 2 N. Imanaka, T. Murata, T. Kawasato and G. ya Adachi, *Sens. Actuators, B*, 1993, **13**, 476–479.
- 3 Y. N. Pal'yanov, A. G. Sokol, Y. M. Borzdov, A. F. Khokhryakov, A. F. Shatsky and N. V. Sobolev, *Diamond Relat. Mater.*, 1999, **8**, 1118–1124.
- 4 J. Zemann, *Acta Crystallogr.*, 1957, **10**, 664–666.
- 5 H. Effenberger and J. Zemann, *Z. Kristallogr. - Cryst. Mater.*, 1979, **150**, 133–138.
- 6 C. J. De Pater and R. B. Helmholtz, *Phys. Rev. B*, 1979, **19**, 5735.
- 7 M. Dušek, G. Chapuis, M. Meyer and V. Petricek, *Acta Crystallogr., Sect. B: Struct. Sci.*, 2003, **59**, 337–352.
- 8 F. Tuinstra, *Z. Kristallogr. - Cryst. Mater.*, 1986, **177**, 155–164.
- 9 I. P. Swainson, M. T. Dove and M. J. Harris, *J. Phys.: Condens. Matter*, 1995, **7**, 4395.
- 10 A. V. Yatsenko, S. G. Zhukov, V. A. D'yakov, A. Etz, W. Molleman and H. Schenk, *Mater. Res. Bull.*, 1995, **30**, 739–744.
- 11 A. V. Yatsenko, S. G. Zhukov, V. A. D'yakov and H. Schenk, *Acta Crystallogr., Sect. C: Cryst. Struct. Commun.*, 1996, **52**, 1–3.
- 12 S. G. Zhukov, A. V. Yatsenko, V. V. Chernyshev, V. A. D'yakov, R. L. Loux and H. Schenk, *Z. Kristallogr. - Cryst. Mater.*, 1999, **214**, 255–258.
- 13 Y. Idemoto, J. W. Richardson Jr, N. Koura, S. Kohara and C.-K. Loong, *J. Phys. Chem. Solids*, 1998, **59**, 363–376.
- 14 A. Kirfel, H. Euler, B. Barbier, E. Hägele and H. Klapper, *Z. Kristallogr. - Cryst. Mater.*, 2000, **215**, 744–751.
- 15 A. Reisman, *J. Am. Chem. Soc.*, 1958, **80**, 3558–3561.
- 16 W. Klement Jr and L. H. Cohen, *Ber. Bunsenges. Phys. Chem.*, 1975, **79**, 327–334.
- 17 A. N. Khlapova and E. S. Kovaleva, *J. Struct. Chem.*, 1967, **7**, 528–532.
- 18 H. C. Stober, *Analytical Profiles of Drug Substances*, Elsevier, 1986, vol. 15, pp. 367–391.
- 19 D. N. Sagatova, N. E. Sagatov, P. N. Gavryushkin, M. V. Banaev and K. D. Litasov, *Cryst. Growth Des.*, 2021, **21**, 6744–6751.
- 20 Ž. Čančarevič, J. Schön and M. Jansen, *Z. Anorg. Allg. Chem.*, 2006, **632**, 1437–1448.
- 21 P. N. Gavryushkin, S. V. Rashenko, A. F. Shatskiy, K. D. Litasov and A. I. Ancharov, *J. Struct. Chem.*, 2016, **57**, 1485–1488.
- 22 P. N. Gavryushkin, A. Behtenova, Z. I. Popov, V. V. Bakakin, A. Y. Likhacheva, K. D. Litasov and A. Gavryushkin, *Cryst. Growth Des.*, 2016, **16**, 5612–5617.
- 23 P. N. Gavryushkin, A. Bekhtenova, S. S. Lobanov, A. Shatskiy, A. Y. Likhacheva, D. Sagatova, N. Sagatov, S. V. Rashchenko, K. D. Litasov, I. S. Sharygin, A. F. Goncharov, V. B. Prakapenka and Y. Higo, *Minerals*, 2019, **9**, 599.
- 24 P. N. Gavryushkin, N. E. Sagatov, D. N. Sagatova, A. Bekhtenova, M. V. Banaev, E. V. Alexandrov and K. D. Litasov, *Cryst. Growth Des.*, 2023, **23**, 6589–6596.
- 25 A. Grzechnik, P. Bouvier and L. Farina, *J. Solid State Chem.*, 2003, **173**, 13–19.
- 26 B. Ying, J. R. Fitzpatrick, Z. Teng, T. Chen, T. W. B. Lo, V. Siozios, C. A. Murray, H. E. Brand, S. Day, C. C. Tang, R. S. Weatherup, M. Merz, P. Nagel, S. Schuppler, M. Winter and K. Kleiner, *Chem. Mater.*, 2023, **35**, 1514–1526.
- 27 C. L. Bull, N. P. Funnell, M. G. Tucker, S. Hull, D. J. Francis and W. G. Marshall, *High Pressure Res.*, 2016, **36**, 493–511.
- 28 S. J. Clark, M. D. Segall, C. J. Pickard, P. J. Hasnip, M. J. Probert, K. Refson and M. C. Payne, *Z. Kristallogr. - Cryst. Mater.*, 2005, **220**, 567–570.
- 29 B. J. Campbell, H. T. Stokes, D. E. Tanner and D. M. Hatch, *J. Appl. Crystallogr.*, 2006, **39**, 607–614.



- 30 H. T. Stokes, D. M. Hatch and B. J. Campbell, ISODISTORT, ISOTROPY Software Suite Online, Accessed: April 2025, <https://iso.byu.edu>.
- 31 O. Arnold, J. C. Bilheux, J. M. Borreguero, A. Buts, S. I. Campbell, L. Chapon, M. Doucet, N. Draper, R. Ferraz Leal, M. A. Gigg, V. E. Lynch, A. Markvardsen, D. J. Mikkelsen, R. L. Mikkelsen, R. Miller, K. Palmen, P. Parker, G. Passos, T. G. Perring, P. F. Peterson, S. Ren, M. A. Reuter, A. T. Savici, J. W. Taylor, R. J. Taylor, R. Tolchenov, W. Zhou and J. Zikovskiy, *Nucl. Instrum. Methods Phys. Res., Sect. A*, 2014, **764**, 156–166.
- 32 J. Rodríguez-Carvajal, *Phys. B*, 1993, **192**, 55–69.
- 33 M. J. Cliffe and A. L. Goodwin, *J. Appl. Crystallogr.*, 2012, **45**, 1321–1329.
- 34 G. Shen, Y. Wang, A. Dewaele, C. Wu, D. E. Fratanduono, J. Eggert, S. Klotz, K. F. Dziubek, P. Loubeyre, O. V. Fat'yanov, P. D. Asimow, T. Mashimo, R. M. M. Wentzcovitch and other members of the IPPS task group, *High Pressure Res.*, 2020, **40**, 299–314.
- 35 H. J. Monkhorst and J. D. Pack, *Phys. Rev. B*, 1976, **13**, 5188–5192.
- 36 J. P. Perdew, A. Ruzsinszky, G. I. Csonka, O. A. Vydrov, G. E. Scuseria, L. A. Constantin, X. Zhou and K. Burke, *Phys. Rev. Lett.*, 2008, **100**, 136406.
- 37 O. V. Dolomanov, L. J. Bourhis, R. J. Gildea, J. A. Howard and H. Puschmann, *Appl. Crystallogr.*, 2009, **42**, 339–341.
- 38 G. M. Sheldrick, *Acta Crystallogr., Sect. A: Found. Adv.*, 2015, **71**, 3–8.
- 39 L. J. Bourhis, O. V. Dolomanov, R. J. Gildea, J. A. K. Howard and H. Puschmann, *Acta Crystallogr., Sect. A: Found. Adv.*, 2015, **71**, 59–75.
- 40 S. Klotz, J. M. Besson and G. Hamel, *High Pressure Res.*, 2006, **26**, 277–282.
- 41 S. Klotz, L. Paumier, G. L. March and P. Munsch, *High Pressure Res.*, 2009, **29**, 649–652.
- 42 D. M. Hatch and H. T. Stokes, *J. Appl. Crystallogr.*, 2003, **36**, 951–952.
- 43 H. T. Stokes, D. M. Hatch and B. J. Campbell, INVARIANTS, ISOTROPY Software Suite Online, accessed: April 2025, <https://stokes.byu.edu/iso/isotropy.php>.
- 44 N. Koura, S. Kohara, K. Takeuchi, S. Takahashi, L. A. Curtiss, M. Grimsditch and M.-L. Saboungi, *J. Mol. Struct.*, 1996, **382**, 163–169.
- 45 M. H. Brooker and J. B. Bates, *J. Chem. Phys.*, 1971, **54**, 4788–4796.
- 46 Y. Hase and I. V. P. Yoshida, *Spectrochim. Acta A*, 1978, **35**, 377–378.
- 47 Y. Hase and I. V. P. Yoshida, *Spectrochim. Acta A*, 1978, **35**, 379.
- 48 R. J. Angel and U. Bismayer, *Acta Crystallogr., Sect. B: Struct. Sci.*, 1999, **55**, 896–901.
- 49 A. B. Cairns and A. L. Goodwin, *Phys. Chem. Chem. Phys.*, 2015, **17**, 20449–20465.
- 50 Y. Zhu, Y. Chen, J. Chen, J. Yin, Z. Sun, G. Zeng, X. Wu, L. Chen, X. Yu, H. Luo, *et al.*, *Adv. Mater.*, 2024, **36**, 2312159.
- 51 S. Wang, N. J. Szymanski, Y. Fei, W. Dong, J. N. Christensen, Y. Zeng, M. Whittaker and G. Ceder, *Inorg. Chem.*, 2024, **63**, 13576–13584.
- 52 C. W. Wilson, C. J. Ridley, S. G. MacLeod and C. L. Bull, *High Pressure Res.*, 2021, **41**, 14–26.
- 53 C. L. Bull, C. J. Ridley, N. P. Funnell, C. W. Wilson and S. G. MacLeod, *Mater. Adv.*, 2021, **2**, 5096–5104.
- 54 D. Li and H. Zhou, *Mater. Today*, 2014, **17**, 451–463.
- 55 H. Du, Y. Wang, Y. Kang, Y. Zhao, Y. Tian, X. Wang, Y. Tan, Z. Liang, J. Wozny, T. Li, *et al.*, *Adv. Mater.*, 2024, **36**, 2401482.
- 56 C. J. Ridley, S. Hull, C. L. Bull and N. P. Funnell, *Structural anomalies in lithium carbonate*, STFC ISIS Neutron and Muon Source, 2020, DOI: [10.5286/ISIS.E.RB2010781](https://doi.org/10.5286/ISIS.E.RB2010781).
- 57 C. J. Ridley and J. K. Hinton, Negative linear compressibility and complex phase behaviour in  ${}^7\text{Li}_2\text{CO}_3$ , SNS ORNL, 2025, DOI: [10.14461/oncat.data/2536722](https://doi.org/10.14461/oncat.data/2536722).

